# **Inorganic Chemistry**

pubs.acs.org/IC Article

# Lanthanide Metal—Organic Frameworks Exhibiting Fluoro-Bridged Extended Chains: Synthesis, Crystal Structures, and Magnetic Properties

Marie L. Mortensen, Shubham Bisht, Muhammad Abbas, Hamid Firouzi, Gregory T. McCandless, Michael Shatruk, and Kenneth J. Balkus, Jr\*



Cite This: Inorg. Chem. 2024, 63, 219-228



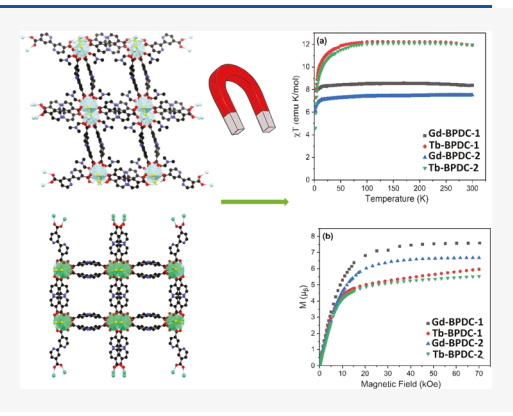
**ACCESS** 

III Metrics & More

Article Recommendations

Supporting Information

**ABSTRACT:** Two fluoro-bridged lanthanide-containing metal—organic frameworks (MOFs) were synthesized using 2,2′-bipyridine-4,4′-dicarboxylic acid (BPDC), a fluorinated modulator, and a lanthanide nitrate. The syntheses of MOFs containing Gd³+ or Tb³+ and a closely related MOF structure containing Ho³+, Gd³+, or Tb³+ are presented. The presence of the fluorinated metal chains in these MOFs is shown through single crystal X-ray diffraction, energy dispersion X-ray spectroscopy, <sup>19</sup>F nuclear magnetic resonance, and X-ray photoelectron spectroscopy. Magnetic measurements reveal weak antiferromagnetic exchange between the Ln³+ ions mediated by fluoride anions along the zigzag ladder chains present in the crystal structures of these MOFs.



#### **■ INTRODUCTION**

Metal—organic frameworks (MOFs) comprise a group of permanently porous crystalline materials. MOFs contain metal ions or clusters connected through organic linkers and have been extensively studied for gas separations, gas adsorption, catalysis, drug delivery, and sensors. Lanthanide MOFs exhibit a large range of topologies due to their low stereochemical preferences and high coordination numbers. Many lanthanides such as Eu<sup>3+</sup> and Tb<sup>3+</sup> have distinct excitation and emission peaks, have distinct excitation and emission peaks, the make them attractive for applications that involve luminescence. Other lanthanides are known for their enhanced magnetic properties.

The popular modulator, 2-fluorobenzoic acid (2-fba), has been widely used to create lanthanide MOFs containing nona-, <sup>12,13</sup> hexa-, <sup>14–16</sup> and triclusters. <sup>5</sup> The formation of such clusters can increase the chemical and thermal stability of the Ln MOFs. <sup>5,14–16</sup> Recently, it was reported that lanthanides react with the 2-fba and extract fluoride, <sup>17,18</sup> which becomes incorporated into the MOF structures as fluoro-bridges between the metal ions. <sup>19–25</sup> For example, Ho-UiO-66 contains a fluoro-bridged hexanuclear cluster when prepared using 2-fba. <sup>18</sup>

Lanthanide MOFs are known for their selectivity toward  ${\rm CO_2}$ . The Lewis acidic nature of lanthanides and open metal sites favor the adsorption of and selectivity for  ${\rm CO_2}$ . Fluoride groups on the linker as well as bonded to the metal ion increases the MOF selectivity for  ${\rm CO_2}$ . Additionally, the

overall thermal stability of these structures may be enhanced by addition of the fluoro-bridges.<sup>31</sup>

The formation of these fluoro-bridged metal clusters allows for closer interactions between the metal centers within the structure. In the absence of fluorinating agents, the lanthanide MOFs typically contain metal dimers with distances further than 4 Å between the nodes, meaning there is very little interaction between the metal ions.32-34 The formation of metal clusters reduces the m-m distance. The addition of fluoro-bridging in the cluster further decreases the distance between metal ions as the metal-fluoride bond is on average shorter than the metal-oxygen bond. There have been several studies on how the addition of fluoro-bridging within lanthanide complexes changes the magnetic coupling between the lanthanide ions. 37,38 Additionally, clusters increase the concentration of the metal ions and help increase the overall magnetic susceptibility of the MOF.<sup>39</sup> In this regard, the Gd<sup>3+</sup>, Tb<sup>3+</sup>, and Dy<sup>3+</sup> ions possess the highest magnetic moments among lanthanides and typically allow realization of interesting magnetic properties in various molecule-based materials.<sup>40–43</sup>

Received: September 1, 2023 Revised: December 6, 2023 Accepted: December 7, 2023 Published: December 27, 2023





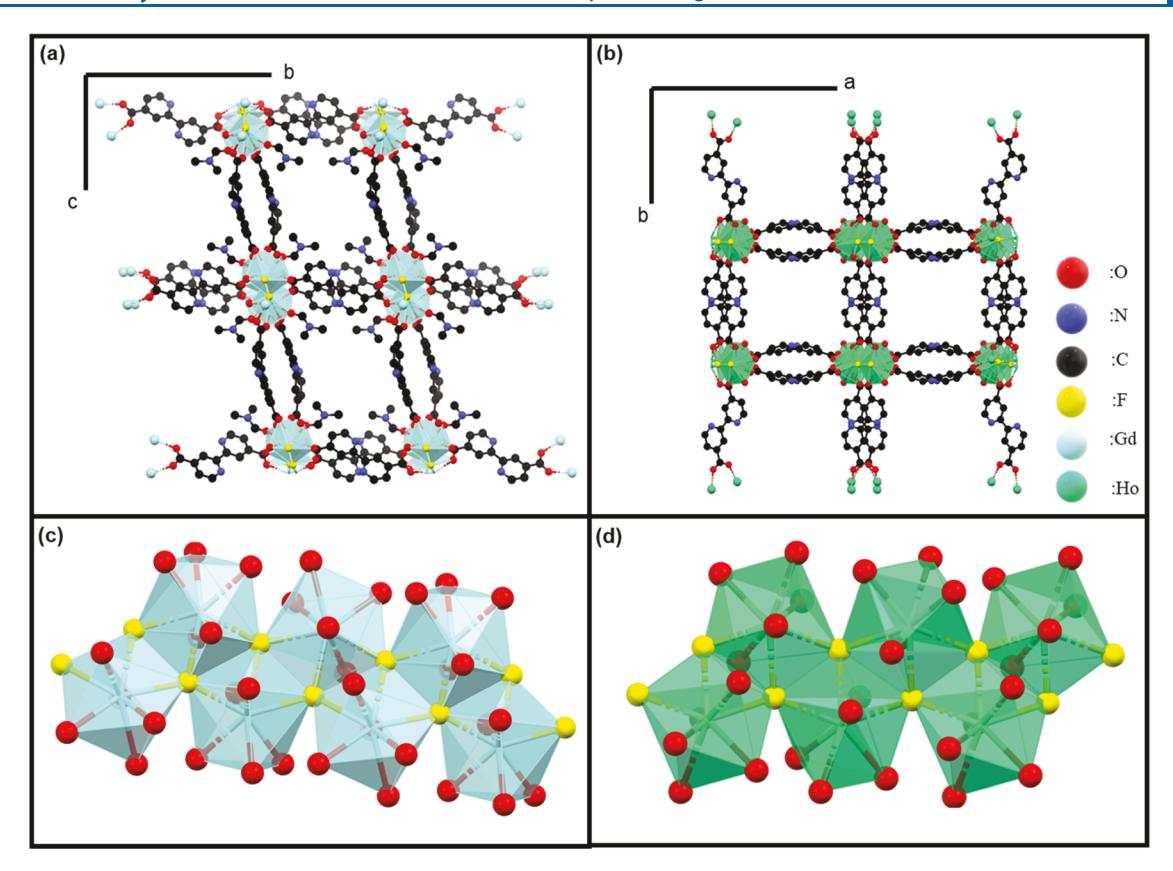


**Figure 1.** Comparison between **Gd-BPDC-1** shown along the *a*-axis (a), **Ho-BPDC-2** shown along the *c*-axis (b), the extended metal chain for **Gd-BPDC-1** (c), and the extended metal chain for **Ho-BPDC-2** (d).

Herein the synthesis, structure, and properties of a fluoror i d g e d  $\,$  G d  $^{3}$   $^{+}$   $\,$  M O F ,  $\,$  G d - B P D C - 1 b r i d g e d  $\,$  G d  $^3$  +  $\,$  M O F ,  $\,$  G d - B P D C - 1  $\,$  (Gd<sub>2</sub>F<sub>2</sub>(C<sub>12</sub>H<sub>6</sub>N<sub>2</sub>O<sub>4</sub>)<sub>2</sub>(C<sub>3</sub>H<sub>7</sub>NO)<sub>2</sub>), and Tb<sup>3+</sup> MOF, Tb-**BPDC-1**  $(Tb_2F_2(C_{12}H_6N_2O_4)_2(C_3H_7NO)_2)$ , isostructural with the Ho-BPDC MOF that has been reported recently.<sup>18</sup> The discovery of a new MOF containing either Ho<sup>3+</sup>, Gd<sup>3+</sup>, or Tb<sup>3+</sup> was labeled as Ho-BPDC-2 (HoF( $C_{12}H_6N_2O_4$ )( $H_2O$ )), Gd-BPDC-2 (GdF( $C_{12}H_6N_2O_4$ )( $H_2O$ )), and Tb-BPDC-2 (TbF( $C_{12}H_6N_2O_4$ )( $H_2O$ )), respectively. MOFs **Gd-BPDC-1** and Tb-BPDC-1 were formed using 2-fba while MOFs Ho-BPDC-2, Gd BPDC-2, and Tb-BPDC-2 were synthesized using 2,6-difluorobenzoic acid (2,6-dfba) or 2-fba. The presence of fluoro-bridged metal chains was verified by single crystal X-ray diffraction (SC-XRD), <sup>19</sup>F nuclear magnetic resonance (19F NMR), X-ray photoelectron spectroscopy (XPS), and energy dispersive X-ray spectroscopy (EDS). The thermal stability, porosity, and physical and chemical characteristics of these MOFs, as well as their magnetic properties are presented.

# ■ RESULTS AND DISCUSSION

**Synthesis.** The reaction of Ln(III) nitrate (Ln =  $Gd^{3+}$  and  $Tb^{3+}$ ), 2,2'-bipryidine-4,4'-dicarboxylic acid (BPDC), and 2-fba in a solution of *N*,*N*-dimethylformamide (DMF) and water resulted in the formation of MOFs **Gd-BPDC-1** and **Tb-BPDC-1**. The modulator, 2,6-dfba or 2-fba, was reacted with Ln(III) nitrate (Ln =  $Gd^{3+}$ ,  $Ho^{3+}$ , and  $Tb^{3+}$ ) and BPDC in a solution of DMF to produce pure MOF **2**. Nitric acid was added to the solution to slow the crystallization of the MOFs.

**Single Crystal XRD.** The crystal structure of **Gd-BPDC-1** contains two crystallographically unique 8-coordinate Gd

metal centers with a distorted square antiprism-shaped local coordination environment. The coordination of both Gd metal centers includes four carboxylate oxygen atoms from the BPDC linkers, three  $\mu_3$ -F linkers, and one oxygen atom of a DMF ligand. The bond lengths are shown in Tables S1–S3.

The closest Gd···Gd interatomic distances are Gd1–Gd1 3.7792 (7) Å, Gd2–Gd2 3.8114 (7) Å, and Gd1–Gd2 3.9519 (7) Å. The two shortest Gd···Gd interatomic distances are between Gd metal centers crystallographically equivalent by symmetry and bridged by both  $\mu_3$ -F linkers and BPDC linkers. The longer Gd···Gd interatomic distance is between Gd metal centers that are crystallographically unique and are bridged only by  $\mu_3$ -F linkers. Excluding all the other element types, the Gd and F atoms coordinate to form wavy zigzag ladders that propagate along the crystallographic a-axis. The overall MOF structure is formed by cross-linking these ladders through the BPDC linkers.

For the crystal structure of the **Ho-BPDC-2**, there is only one crystallographically unique, 8-coordinate Ho metal center with a distorted square antiprism-shaped local coordination environment. Similar to the crystal structure described above, this coordination environment includes four carboxylate oxygen atoms from the BPDC linkers, three  $\mu_3$ -F linkers, and one oxygen atom of a H<sub>2</sub>O ligand. The bond lengths are shown in Tables S4–S6.

The closest Ho···Ho interatomic distances are 3.7410 (7) and 3.8115 (8) Å. The shortest Ho···Ho interatomic distance is between Ho metal centers that are bridged by both  $\mu_3$ -F linkers and BPDC linkers while the longer Ho···Ho interatomic distance is between Ho metal centers that are only bridged by  $\mu_3$ -F linkers. Similar to the crystal structure of

**Gd-BPDC-1**, the Ho and F atoms coordinate to also form wavy zigzag ladders that propagate along the crystallographic *c*-axis and are cross-linked by the BPDC linkers into a framework material.

The differences between the crystal structures of Gd-BPDC-1 and Ho-BPDC-2 can be seen best in the unit cell representations. The relationship between the structures can be best seen when the crystal packing of Gd-BPDC-1 is viewed along the *a*-axis and that of Ho-BPDC-2 is viewed along the *c*-axis, as shown in Figure 1. The view along the *b*-axis is similar in both MOFs as shown in Figure S2 and shows the wavy zigzag ladders that appear in both MOFs (Table 1).

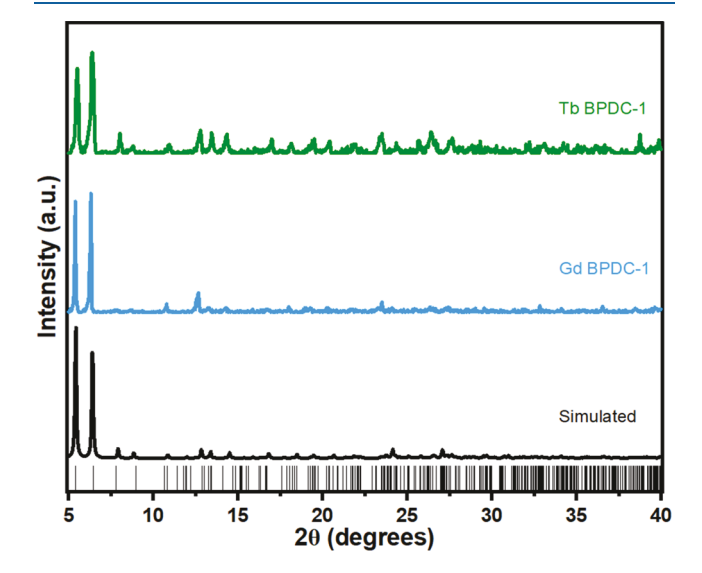
**Determining Thermal Stabilities.** The thermal stabilities of MOFs 1 and 2 were determined through thermogravimetric analysis (TGA, Figure S3). All five MOFs are thermally stable up to 480 °C, at which point they begin to decompose to oxides. The TGA curves are very similar, revealing the initial mass loss from absorbed water and any uncoordinated DMF

Table 1. Single Crystal Data for Gd-BPDC-1 and Ho-BPDC-2

	Gd-BPDC-1	Ho-BPDC-2
CCDC number	2090144	2090145
chemical formula	$Gd_{2}F_{2}(C_{12}H_{6}N_{2}O_{4})_{2}(C_{3}H_{7}NO)_{2}$	$\begin{array}{c} HoF(C_{12}H_6N_2O_4) \\ (H_2O)\cdot 2(C_2H_6O)\cdot \\ H_2O \end{array}$
formula weight (g/mol)	983.07	554.28
T (K)	105	105
crystal system	triclinic	monoclinic
space group	$P\overline{1}$	P2/c
a (Å)	8.4385 (16)	16.593 (4)
b (Å)	14.090 (3)	14.005 (3)
c (Å)	16.497 (3)	8.5357 (13)
$\alpha$ (deg)	81.641 (6)	
$\beta$ (deg)	88.678 (6)	91.037 (12)
γ (deg)	79.384 (10)	
$V(Å^3)$	1907.4 (7)	1983.3 (7)
Z	2	4
crystal size (mm)	$0.15 \times 0.08 \times 0.07$	$0.15 \times 0.03 \times 0.03$
F (000)	948	1088
M	983.07	554.28
λ (Å)	0.71073	0.71073
$\mu \text{ (Mo K}\alpha) \text{ (mm}^{-1})$	3.51	4.04
reflections measured	11,669	57,806
independent reflections	11,669	6090
reflections with $I > 2\sigma(I)$	10,194	4940
parameters	456	263
$R_{ m int}$	0.050	0.076
final $R$ value $(I > 2\sigma(I))$	0.030	0.032
final $R_w(F^2)$ $(I > 2\sigma(I))$	0.078	0.056
final R value (all data)	0.040	0.049
final $R_w$ $(F^2)$ (all data)	0.081	0.061
goodness of fit on $F^2$	1.10	1.03

until 150 °C. The secondary drop, present in all curves from 220 to 330 °C, most likely is caused by uncoordinated linker, coordinated solvent, and trapped 2-fba. The possible presence of trapped 2-fba is demonstrated through <sup>19</sup>F NMR. Figure S4 shows the presence of 2-fba with a peak at –112.28 ppm in the dissolved MOF Ho-BPDC-2 in the as-synthesized sample. The removal of 2-fba once activated at 220 °C is demonstrated in Figure S5. The <sup>1</sup>H NMR spectra for activated Gd-BPDC-1 and Gd-BPDC-2 are shown in Figures S6 and S7. They do not show the presence of excess 2-fba in the samples.

The phase purity and thermal stability were determined by powder XRD and TGA. Figure 2 shows the experimental and



**Figure 2.** Experimental PXRD of **Gd-BPDC-1** and **Tb-BPDC-1** compared with the simulated pattern.

simulated patterns for MOFs Gd-BPDC-1 and Tb-BPDC-1, which match without any additional peaks, indicating high purity. After the MOFs were washed and activated to 130 °C (the first weight loss shown in the TGA), there is no change in the structure, as shown in Figures S8 and S9. However, there is a change in the structure when the two MOFs are heated to 220 °C (the final drop in the TGA before decomposition).

The XRD patterns of Ho-BPDC-2, Gd-BPDC-2, and Tb-BPDC-2 match the one simulated by using the Ho MOF structure, as shown in Figure 3, thus indicating the isostructural nature of these Ho, Gd, and Tb MOFs. The three structures are stable after washing with DMF and activated at 130  $^{\circ}$ C to remove the excess DMF and 2-fba from the pores. However, when heated to 220  $^{\circ}$ C, there is a structural change, as shown in Figures S10–S12.

**Presence of Fluorine.** The presence of fluorine in the MOFs was verified by energy dispersion spectroscopy (EDS). The EDS spectra for the as-synthesized and activated MOFs are shown in Figures S13—S17. The activated samples were washed with DMF several times over the course of two to three days and then heated to 130 °C under vacuum. This process was used to remove any 2-fba remaining in the pores. All three MOFs show the presence of fluorine in both assynthesized and activated samples. All as-synthesized samples show an excess amount of fluorine, which can be attributed to 2-fba remaining in the pores. For **Gd-BPDC-1**, the theoretical ratio of gadolinium to fluorine is 8.3. The experimental ratio of 11.3 was found in the activated sample, indicating that there is

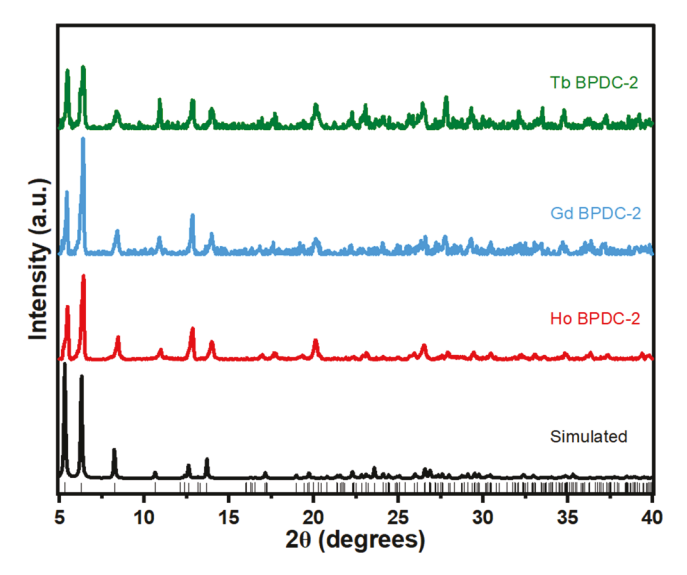


Figure 3. PXRD patterns of Ho-BPDC-2, Gd-BPDC-2, and Tb-BPDC-2 compared to the simulated pattern.

a mixture of OH and F bridging. A similar trend is found in the other four MOFs as shown in Tables 2 and 3. Previously, several papers have indicated the possible presence of a mixed hydroxy-bridged and fluoro-bridged cluster. The ratios found from EDS do not give any indication that there is a lack of fluorine due to replacement of fluorides with hydroxides in MOFs Ho-BPDC-2, and Tb-BPDC-2. Gd-BPDC-1, Gd-BPDC-2, and Tb-BPDC-1 show a minor deficiency in fluorine content, which indicates that some hydroxy/oxy bridges might be present.

The presence of possible hydroxy-bridging was analyzed through Fourier-transform infrared spectroscopy (FT-IR) spectroscopy. When hydrogen bonding is removed a sharp peak for OH will appear between 3630 and 3680 cm<sup>-1</sup>. <sup>48</sup>, <sup>49</sup> When the activated samples of MOFs 1 and 2 were prepared as dried IR pellets, they produced the FT-IR spectra shown in Figure S18. These spectra do not show a sharp peak for hydroxy-bridging. However, EDS and FT-IR have limited sensitivity, and there is a possibility of a small fraction of oxyor hydroxy-bridging present in all samples, which can be verified by X-ray photoelectron spectroscopy (XPS).

XPS was used to determine the presence of elements and their chemical states in the MOFs. XPS spectra were taken from the activated samples of each MOF. The XPS survey spectrum for each MOF, as shown in Figure S19, indicates the presence of C, F, O, N, and Ln (Ln = Ho, Gd, and Tb). As shown in Figure 4a, the high-resolution F 1s spectrum for Gd-BPDC-1 has a binding energy of 684.8 eV. This value is the same as the binding energy of GdF<sub>3</sub> and lower than the binding energy of 688.5 eV for the C–F bond found in 2-

fba. <sup>23,50</sup> This indicates that the F<sup>-</sup> anion is bound to the Gd<sup>3+</sup> and not carbon. The F 1s spectra for MOFs Tb-BPDC-1, Ho-BPDC-2. Gd-BPDC-2 and Tb-BPDC-2 also show the presence of this metal-fluoride bond as seen in Figure S20. The F 1s spectrum for Tb-BPDC-2 is very similar to that of Gd-BPDC-1 with a binding energy of 685.6 eV. The F 1s spectra for Ho-BPDC-2, Gd-BPDC-2, and Tb-BPDC-2 show similar binding energies of 685.2, 684.8, and 685.3 eV, respectively. These signals correspond to fluorine incorporated into the cluster and not to fluorine from 2-fba in the pores or MOFs. The high-resolution O 1s spectra were also acquired for all samples as shown in Figures 4 and S21. As shown in Figure 4b, Gd-BPDC-1 does not show any indication that there is M-O-M bonding within the structure, within the XPS sensitivity limit.<sup>24</sup> The most prominent peak in the O 1s spectrum is from the C-O-M bond from the carboxylic group binding to the metal. However, spectra of MOFs Tb-BPDC-1, Ho-BPDC-2, Gd-BPDC-2, and Tb-BPDC-2 reveal a small peak between 525 and 530 eV that is indicative of M-O-M binding. The presence of a mixture of OH/F bridging found within these MOFs formed with 2-fba has been observed with other MOFs and appears to be dependent on the metal ion, linkers, and type of organofluorine modulator used. 24,31,46

**Gas Adsorption.** The pores of the MOFs were probed by using  $CO_2$  and  $N_2$ . The five MOFs have one-dimensional (1D) cylindrical pores. When using nitrogen gas, there is very little adsorption in all five MOFs, with Brunauer-Emmett-Teller (BET) surface areas only reaching 12.6  $\pm$  0.2, 6  $\pm$  0.1, 16.1  $\pm$ 0.2, 24.0  $\pm$  0.2, and 2.88  $\pm$  0.06 m<sup>2</sup>/g for Gd-BPDC-1, Tb-BPDC-1, Ho-BPDC-2, Gd-BPDC-2, and Tb-BPDC-2, respectively. This small surface area indicates that the nitrogen is not easily absorbed into the pores. When the pores were probed with CO<sub>2</sub>, as shown in Figure 5, the BET surface areas of  $178 \pm 3$ ,  $162.1 \pm 0.8$ ,  $98 \pm 2$ ,  $171 \pm 1$ , and  $223 \pm 2$  m<sup>2</sup>/g were measured for MOFs Gd-BPDC-1, Tb-BPDC-1, Ho-BPDC-2, Gd-BPDC-2, and Tb-BPDC-2, respectively. The amount of CO<sub>2</sub> absorbed within these MOFs is 3.3 wt % for Gd-BPDC-1, 4.0 wt % for Tb-BPDC-1, 3.9 wt % for Ho-BPDC-2, 4.3 wt % for Gd-BPDC-2, and 5.0 wt % for Tb-BPDC-2.51

**Magnetic Properties.** The temperature dependence of magnetic susceptibility  $(\chi)$  was measured on microcrystalline nonactivated samples of Gd-BPDC-1, Tb-BPDC-1, Gd-BPDC-2, and Tb-BPDC-2. At higher temperatures, all samples showed nearly temperature-independent values of the  $\chi T$  product (Figure 6a) and linear dependences of  $1/\chi$  vs T (Figure S27). The latter was fit to the Curie—Weiss law,  $1/\chi = (T-\theta)/C$ , where  $\theta$  is the Weiss constant, related to the nearest-neighbor magnetic exchange coupling, and C is the Curie constant, defined as

Table 2. EDS Weight Percentages of Each MOF before Activation

elements	Gd-BPDC-1 wt %	Tb-BPDC-1 wt %	Ho-BPDC-2 wt %	Gd-BPDC-2 wt %	Tb-BPDC-2 wt %
С	41.8	55.9	40.5	41.0	44.0
N	6.3	16.7	6.8	4.8	8.6
O	16.0	5.9	15.3	13.1	17.0
F	4.7	3.1	5.6	7.2	4.1
Ln	31.2	18.4	31.8	33.9	26.3
total	100.0	100.0	100.0	100.0	100.0
Ln:F	6.7	5.9	5.7	4.7	6.4

Table 3. EDS Weight Percentages of Each MOF after Activation

elements	Gd-BPDC-1 Act wt %	Tb-BPDC-1 Act wt %	Ho-BPDC-2 Act wt %	Gd-BPDC-2 Act wt %	Tb-BPDC-2 Act wt %
С	54.7	41.5	45.0	38.8	41.4
N	5.5	6.5	5.9	6.8	7.9
O	18.6	15.4	16.0	15.1	16.5
F	1.7	2.1	3.8	2.9	3.8
Ln	19.6	34.5	29.3	36.4	30.5
total	100.0	100.0	100.0	100.0	100.0
Ln:F	11.5	16.4	7.7	12.6	8.0

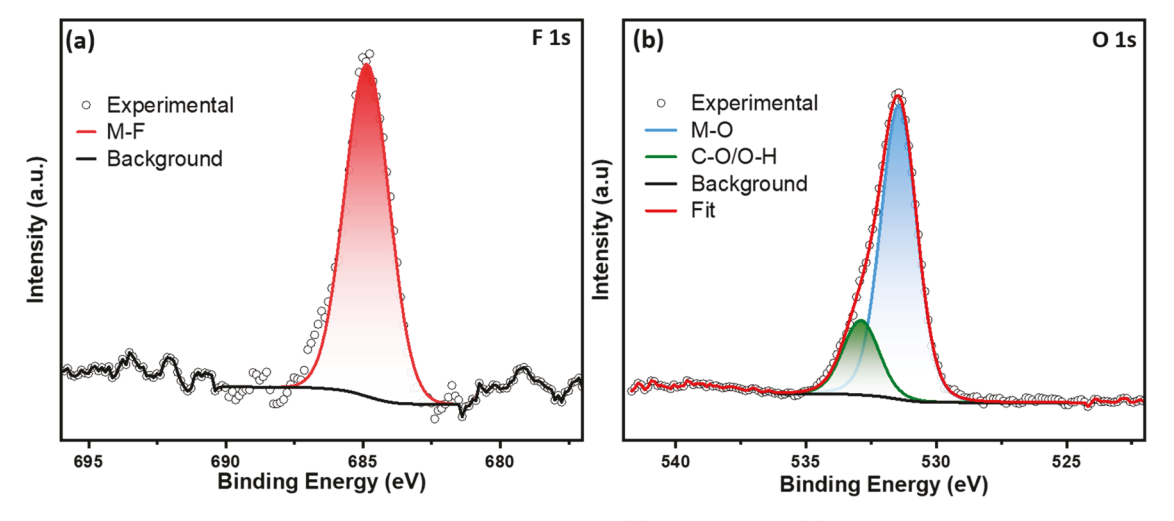


Figure 4. These XPS spectra show the high-resolution spectra for the F 1s (a) and the O 1s (b) for MOF Gd-BPDC-1.

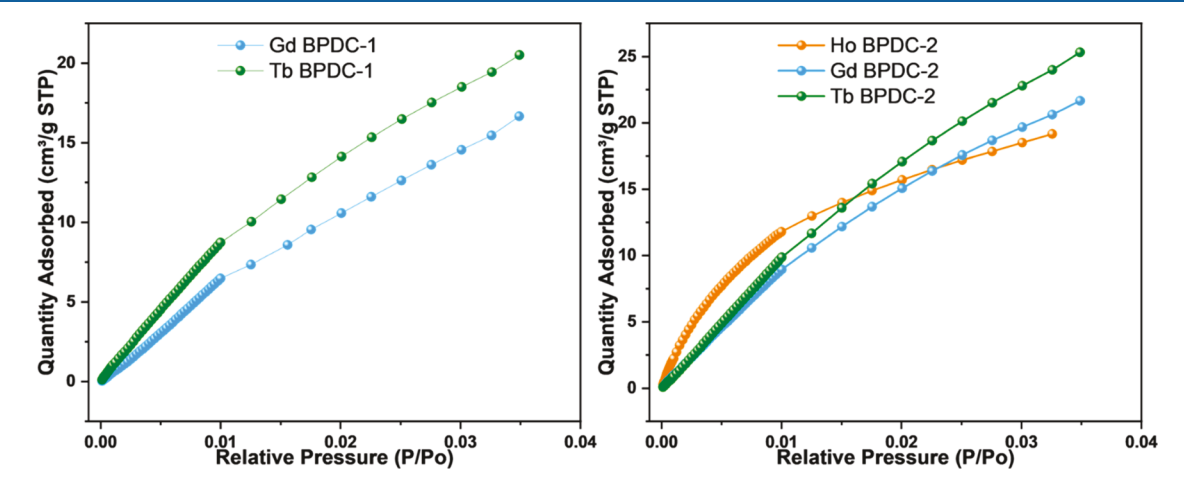


Figure 5. CO<sub>2</sub> Adsorption data for the MOFs Gd-BPDC-1 and Tb-BPDC-1 (a), and (b) shows the CO<sub>2</sub> adsorption data for MOFs Ho-BPDC-2, Gd-BPDC-2, and Tb-BPDC-2.

$$C = \frac{N\mu_{\rm B}^2 g^2 J(J+1)}{3k}$$
 (1)

where N is Avogadro's number,  $\mu_{\rm B}$  is Bohr magneton, g is the Lande g-factor, k is the Boltzmann constant, and J is the total angular momentum in the ground state of the corresponding  ${\rm Ln^{3+}}$  ion. The best-fit C values are in good agreement with those expected for the  ${\rm Ln^{3+}}$  ions in the free-ion approximation (Table 4). The field-dependent magnetization measured at 1.8 K (Figure 6b) shows saturation values close to the expected 7  $\mu_{\rm B}$  for the  ${\rm Gd^{3+}}$  ions in the case of  ${\rm Gd\text{-}BPDC\text{-}1}$  and  ${\rm Gd\text{-}BPDC\text{-}2}$ , while for  ${\rm Tb\text{-}BPDC\text{-}1}$  and  ${\rm Tb\text{-}BPDC\text{-}2}$ , the maximum magnetization observed at 7 T is substantially

lower than the 9  $\mu_B$  expected for the Tb<sup>3+</sup> ion (Table 4). This discrepancy will be discussed below.

The Gd-containing MOFs Gd-BPDC-1 and Gd-BPDC-2 show a decrease in  $\chi T$  only at very low temperatures (Figure 6a), suggesting weak antiferromagnetic (AFM) coupling between the Gd<sup>3+</sup> ions. The magnetic behavior can be modeled by considering the zigzag ladders of fluoride-bridged Gd<sup>3+</sup> ions, observed in the crystal structures of Gd-BPDC-1 and Gd-BPDC-2, as infinite chains of S=7/2 magnetic moments. Despite the presence of two crystallographically unique Gd centers, the Gd···Gd distances along the chain are comparable and the magnetic interactions can be approximated by a single magnetic exchange constant  $J_{\rm ex}$  (Figure 7). The temperature dependence of  $\chi$  was fit to the Bonner—

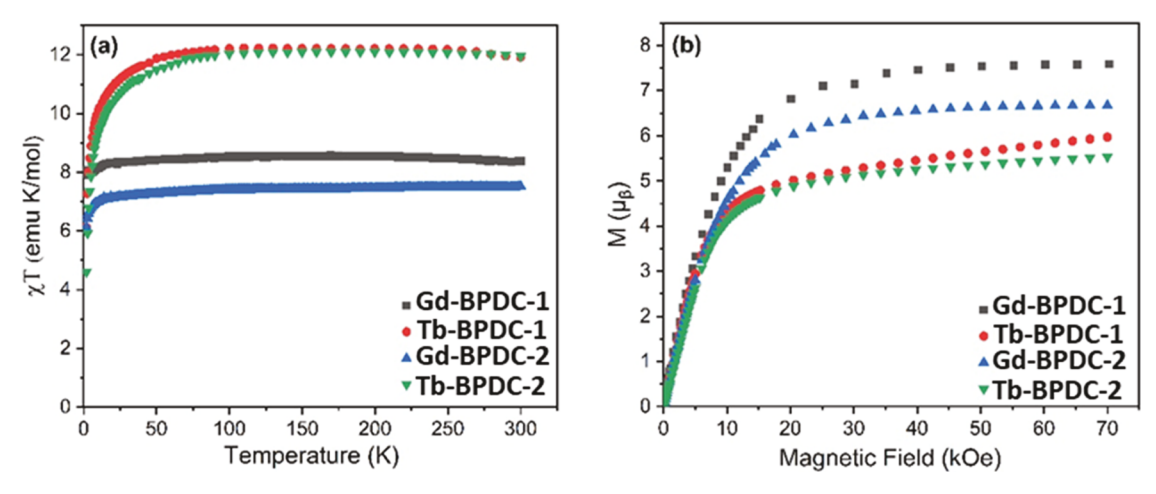


**Figure 6.** Magnetic properties of **Gd-BPDC-1**, **Tb-BPDC-1**, **Gd-BPDC-2**, and **Tb-BPDC-2**: the temperature dependence of  $\chi T$  measured under an applied magnetic field of 1000 Oe (a) and the field dependence of the magnetization measured at 1.8 K (b).

Table 4. Summary of Magnetic Properties for Gd-BPDC-1, Tb-BPDC-1, Gd-BPDC-2, and Tb- BPDC-2

C (emu·K/mol)					
compound	ground state of the Ln3+ ion	theoretical	experimental	$\theta$ (K)	$M_{\rm sat}$ at 70 kOe 1.8 K $(\mu_{\rm B})$
Gd-BPDC-1	<sup>8</sup> S <sub>7/2</sub>	7.875	8.383(9)	1.5(2)	7.59
Tb-BPDC-1	$^{7}\mathrm{F}_{6}$	11.82	11.90(6)	4(1)	5.96
Gd-BPDC-2	${}^{8}S_{7/2}$	7.875	7.554(1)	-2.36(4)	6.67
Tb-BPDC-2	$^{7}\mathrm{F}_{6}$	11.82	11.99(2)	0.9(4)	5.53

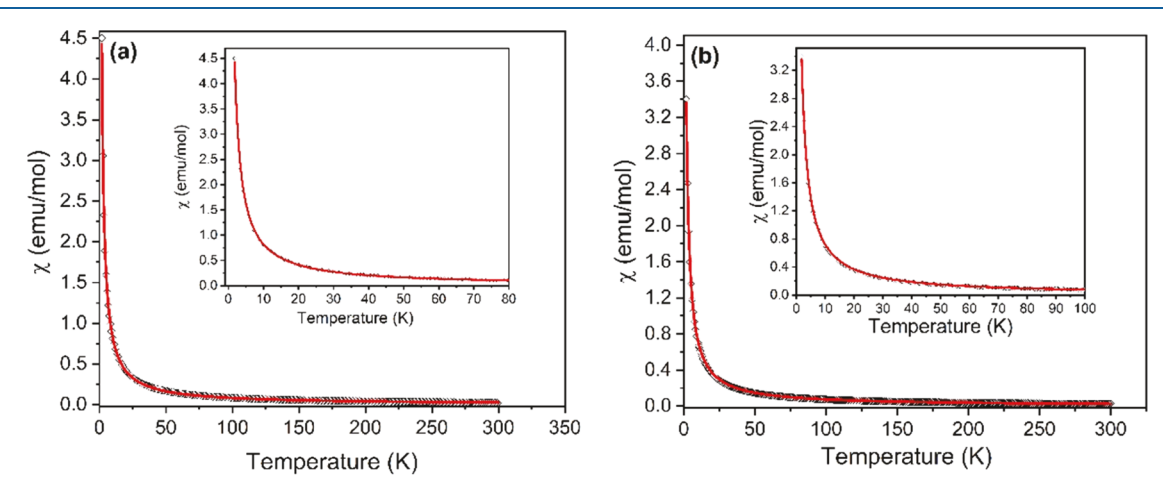


Figure 7. Temperature dependence of  $\chi$  for Gd-BPDC-1 (a) and Gd-BPDC-2 (b). The empty black circle represents experimental data points, while the solid red lines show the best fit to the Bonner-Fisher model (eq 2). The insets show the low-temperature region of the  $\chi$  vs T curves.

Fisher model for the infinite spin chain, which also was applied to other Gd-containing chain compounds. 52,53

$$\chi = \left[ \frac{N\mu_b^2 g^2 S(S+1)}{3kT} \right] \left[ \frac{1+u}{1-u} \right] = \frac{C}{T} \left[ \frac{1+u}{1-u} \right]$$
where  $u = \coth \left[ \frac{2J_{ex}S(S+1)}{kT} \right] - \left[ \frac{kT}{2J_{ex}S(S+1)} \right]$  (2)

which resulted in the best-fit values  $J_{\rm ex} = -0.00085(1)~{\rm cm}^{-1}$  and g = 2.027(1). The *g*-factor is slightly higher than the 1.99–2.01 typically observed for the Gd<sup>3+</sup> ion. Therefore, the value of *g* was fixed at 2, and the modified fit was performed by introducing a scaling factor, (1 + b), as a multiplier in eq 2. The best-fit values obtained were  $J_{\rm ex} = -0.00245(8)~{\rm cm}^{-1}$  and

b=0.05, which correspond to ~5% of paramagnetic impurity. The presence of such an impurity can also be deduced from the slight increase in the  $\chi T$  value at the lowest experimental temperatures, as can be seen in the inset of Figure 7, and from the saturation magnetization of 7.59  $\mu_{\rm B}$  slightly exceeding the theoretically expected value of 7  $\mu_{\rm B}$  for the Gd<sup>3+</sup> ion.

The same model was used to describe the magnetic behavior of **Gd-BPDC-2**, giving the best-fit values  $J_{\rm ex}=-0.01002(3)$  cm<sup>-1</sup> and g=1.9163(3). In this case, the g-factor value is notably lower than 2, suggesting the presence of a diamagnetic impurity. Similar to the procedure described above, the g value was fixed at 2 and the scaling factor was introduced in eq 2. The best-fit values obtained from such a modified fit were  $J_{\rm ex}=-0.01266(5)$  cm<sup>-1</sup> and b=-0.05, indicating  $\sim 5\%$  of diamagnetic impurity (Figure 7a), which is also in agreement with the maximum magnetization value of 6.67  $\mu_{\rm B}$  (at 70 kOe

and 1.8 K) being slightly lower than the value of 7  $\mu_{\rm B}$  expected for the Gd<sup>3+</sup> ion.

The results of magnetic modeling for MOFs Gd-BPDC-1 and Gd-BPDC-2 indicate the presence of weak AFM exchange between the Gd³+ ions along the zigzag ladder. The interaction between the chains is expected to be substantially weaker, essentially negligible, given that the nearest interchain Gd···Gd distance is 13.414 Å. We note that the antiferromagnetic exchange constants of the same order of magnitude were reported for interactions between fluoride-bridged Gd³+ ions in a molecular Gd² dimer ( $J_{\rm ex}=0.062~{\rm cm}^{-1}$ )<sup>SS</sup> and in a pentanuclear Gd³Ga² complex ( $J_{\rm ex}=0.028~{\rm cm}^{-1}$ ). The slightly stronger antiferromagnetic interaction in the former might be explained by a nearly linear Gd–F–Gd angle, which should allow for a better delocalization of spin density across the fluoride bridge.

The  $\chi T$  values for Tb-containing MOFs Tb-BPDC-1 and Tb-BPDC-2 also remain relatively constant at higher temperatures (Figure 7a) but decrease faster below 70 K as compared to those for Gd-BPDC-1 and Gd-BPDC-2. The maximum magnetization values reached at 70 kOe and 1.8 K are 5.96  $\mu_{\rm B}$ for Tb-BPDC-1 and 5.33  $\mu_B$  for Tb-BPDC-2, which are substantially lower than the 9  $\mu_{\rm B}$  expected for the free Tb<sup>3+</sup> ion. It is unlikely that the faster decrease in  $\chi T$  and the suppressed magnetization in the ground state, observed at the lowest experimental temperature, are caused by strong antiferromagnetic exchange since there is an obvious reason why the exchange in the case of these Tb-containing MOFs should be by orders of magnitude stronger than in the isostructural Gdcontaining MOFs. Therefore, it is reasonable to attribute these differences in the magnetic behavior to crystal field effects. In contrast to the magnetically isotropic 4f<sup>7</sup> Gd<sup>3+</sup> ion, the 4f<sup>8</sup> Tb<sup>3+</sup> ion is known to exhibit strong magnetic anisotropy and appreciable crystal field splitting of the I = 6 ground state.<sup>5</sup> Modeling the magnetic behavior of this ion requires a more indepth theoretical analysis, including calculations and measurements of the crystal field splitting pattern, which are beyond the scope of the present work.

# CONCLUSIONS

The compounds 2-fluorobenzoic acid and 2, 6-difluorobenzoic acid, have been widely used as modulators for Ln-based MOFs. However, it is clear that rare earth ions can extract fluorine from a growing list of organofluorine molecules, which can result in bridging fluorides in a MOF structure. The adsorption isotherms for each MOF were collected and indicated that these MOFs could be used for  $\mathrm{CO_2/N_2}$  separation. Magnetic measurements of the Gd- and Tb-containing MOFs reveal weak antiferromagnetic interactions between the metal centers along the zigzag ladders of the fluoride-bridged  $\mathrm{Ln^{3+}}$  ions.

#### **■ EXPERIMENTAL SECTION**

Single Crystal XRD Method. On a Bruker Kappa D8 Quest diffractometer equipped with an  $I\mu$ S Mo Kα radiation source, Oxford Cryosystems cryostream, and a Photon II CPAD detector, low temperature (T=105 K) single crystal X-ray diffraction data sets were collected for the structure determination of Gd-BPDC-1 and Ho-BPDC-2. After the data collection, the data sets were processed (integration with Bruker SAINT and scaled with either Bruker SADABS or TWINABS using multiscan absorption correction) and then evaluated (space group selection using Bruker XPREP). SHELXT (intrinsic phasing method) and SHELXL were used to generate the initial structural models and further refine these models (least-squares method), respectively. All non-hydrogen atoms

(except in the case of disordered solvent EtOH molecules) were refined anisotropically. The refinement of hydrogen atoms was carried out in "riding" (AFIX) atomic sites. Note: The crystal structure of **Gd-BPDC-1** is a 2-component, nonmerohedral twin with a Twin Law of (-0.99994, -0.00021, 0.00010, -0.60501, 1.00017, -0.23981, -0.00087, 0.00197, -1.00023) and a final refined BASF parameter of 0.4123(8).

**Powder X-Ray Diffraction (PXRD).** The PXRD patterns were collected on an Ultima IV X-ray diffractometer (Rigaku) equipped with Cu K $\alpha$  radiation (1.5406 Å) from a long fine-focus copper target by using a 285 mm goniometer scintillation counter as the detector. They were collected using  $\beta$  filter and not a monochromator, with a scan speed of 2 °/min and a step size of 0.04° in  $2\theta$ .

Thermogravimetric Analysis (TGA). The TGA was completed using an SDT Q600 (TA Instruments). The samples were then heated to 900 °C at a rate of 10 °C/min from 30 °C.

Scanning Electron Microscopy/Energy Dispersive X-ray Spectroscopy (SEM/EDS). The SEM/EDS spectra for these samples were performed on a Zeiss EVO LS SEM instrument and an Aztec Instruments Oxford EDS. These samples were not coated with gold or carbon. The samples were activated at 130 °C and washed with DMF three times over the course of two days.

Sample Preparation of Pellets for Fourier-Transform Infrared Spectroscopy (FT-IR). The KBr Pellets were pressed at 10,000 psi and then heated at  $130~^{\circ}\text{C}$  for 1 day under vacuum. The samples were immediately analyzed after removal from the vacuum to reduce water adsorption.

**NMR Instrumentation and Sample Preparation.** The NMR data was collected at 298 K using a Bruker Avance III HD 600 MHz Spectrometer, and it was processed using TopSpin 4.0.1. Residual solvent peaks were utilized as a reference for NMR spectra in  $^{19}\mathrm{F}$  NMR and  $^{1}\mathrm{H}$  NMR. 1 mL of DMSO- $d_6$  was mixed with a 20  $\mu\mathrm{L}$  solution of D<sub>2</sub>O–D<sub>2</sub>SO<sub>4</sub> 40%. The 500  $\mu\mathrm{L}$  DMSO- $d_6$  solution was added to 4 mg of the sample, which was then sonicated for 5 min and kept in a 60 °C oven for 4 h. After that, the solution was poured into the NMR tube.

**X-ray Photoelectron Spectroscopy (XPS).** The XPS data was collected on a PHI VersaProbe II Scanning XPS Microprobe (Physical Electronics Inc., Chanhassen, Minnesota) equipped with an Al  $K_{\alpha}$  X-ray source ( $E_{\rm p}=1486.7~{\rm eV}$ ) at pressure  $1.6\times10^{-9}$  Torr. The high-resolution spectra were collected at the pass energy of 23.5 eV with a step size of 0.2 eV. Photoelectron spectra were obtained using a charge compensation of 2 mA using an electron flood gun. The sample surface was cleaned by sputtering a gas-cluster ion beam (GCIB) with an energy of 10 kV and a cluster size of 2500 atoms. The data was processed with the software CasaXPS and energies were calibrated to adventitious  $C_{1s}$  at 284.8 eV and Au  $4f_{7/2}$  at 83.95 eV.

Gas Adsorption Analysis and Sample Preparation. The samples were prepared for the surface area analysis by submerging them in fresh DMF four times over the course of three days and then activated in a vacuum at 135 °C overnight. The samples were further activated on a micrometrics ASAP 2020 surface area and porosity analyzer for 12 h at 120 °C. The  $\rm N_2$  adsorption isotherms were taken at 77 K using ultrahigh purity (99.999%) nitrogen. The  $\rm CO_2$  adsorption isotherms were taken at 273 K using ultrahigh purity  $\rm CO_2$  (99.999%). The surface area was calculated by the Brunauer–Emmett–Teller (BET) method in the relative pressure ( $P/P_0$ ) range of 0.05–0.30 for  $\rm N_2$  and 0.010 to 0.025 for  $\rm CO_2$ , and pore size distributions were calculated using the nonlocal density functional theory (NLDFT) model.

Magnetic Measurements. Magnetic measurements were performed using a magnetic property measurement system MPMS-XL (Quantum Design) equipped with a superconducting quantum interference device (SQUID). Each polycrystalline sample was loaded into a polycarbonate capsule that was mounted in a plastic straw attached to a sample transport rod. The temperature dependence of magnetic susceptibility was measured in the range of 1.8–300 K in an applied field of 1000 Oe. Field-dependent magnetization measurements were performed at 1.8 K with the magnetic field varying from 0 to 70 kOe. The data were corrected for diamagnetism from the

sample holder and for intrinsic diamagnetism by using tabulated constants.

**Materials.** The chemicals were used as received without any further modifications. Gadolinium nitrate hexahydrate (99.9%) was purchased from Strem Chemicals, holmium(III) nitrate pentahydrate (99.9%) was purchased from Strem Chemicals, terbium(III) nitrate hydrate (99.9%) was purchased from Alfa Aesar, *N,N'*-dimethylformamide (DMF) was purchased from Fisher Chemical, 2,2'-bipryidine-4,4'-dicarboxylic acid (98%) was purchased from CombiBocks, 2,6-difluorobenzoic acid (97%) was purchased from AmBeed, 2-fluorobenzoic acid (97%) was purchased from Aldrich, and concentrated nitric acid (68%) was purchased from Fisher Scientific.

 $C_{30}H_{26}F_2Gd_2N_6O_{10}$  (Gd-BPDC-1). Gadolinium(III) nitrate hexahydrate (91.4 mg, 0.202 mmol), 2,2′-bipyridine-4,4′-dicarboxylic acid (22.5 mg, 0.0921 mmol), and 2-fluorobenzoic acid (244.4 mg, 1.60 mmol) were dissolved in a DMF (11 mL) and water (2.5 mL) solution. Concentrated nitric acid (0.2 mL) was added to the reaction. In a 20 mL scintillation vial, the solution was heated at 120 °C for 24 h. The resulting white rectangular crystals were cooled to room temperature, centrifuged twice with DMF, and air-dried in an 8 $\rm \mathring{o}C$  oven. This resulted in a 26.1% yield.

 $C_{30}H_{26}F_{2}Tb_{2}N_{6}O_{10}$  (*Tb-BPDC-1*). Terbium(III) nitrate hydrate (184.8 mg, 0.4079 mmol), BPDC (55.6 mg, 0.228 mmol), and 2-fba (487.6 mg, 3.480 mmol) were dissolved in DMF (20 mL) and water (5 mL). Concentrated nitric acid (0.2 mL) was added to the solution. In a 40 mL scintillation vial, the solution was heated to 120 °C for 24 h. The white crystals that precipitated out were cooled to room temperature, centrifuged with DMF twice, and air-dried at 80 °C. This resulted in a yield of 39.0%.

 $C_{16}H_{22}FHoN_2O_8$  (Ho-BPDC-2). Holmium(III) nitrate hydrate (92.4 mg, 0.210 mmol), BPDC (21.4 mg, 0.0876 mmol), and 2,6-difluorobenzoic acid (120.3 mg, 0.7609 mmol) were dissolved in DMF (11 mL)/ $H_2O$  (2.5 mL). Concentrated nitric acid (0.2 mL) was added to the solution. In a 20 mL scintillation vial, the solution was heated to 120 °C for 24 h. The yellow/pink rectangular crystals were cooled to room temperature, centrifuged with DMF two times, and air-dried at 80 °C. This resulted in a yield of 80.9%.

Single Crystal Synthesis of  $C_{16}H_{22}$ FHoN<sub>2</sub>O<sub>8</sub> (Ho-BPDC-2). This was formed through a single-crystal transformation. The crystals were first formed using holmium(III) nitrate hydrate (92.4 mg, 0.210 mmols), BPDC (21.4 mg, 0.0876 mmols), and 2-fluorobenzoic acid (243.5 mg, mmols) were dissolved in DMF (11 mL)/H<sub>2</sub>O (2.5 mL). Concentrated nitric acid (0.2 mL) was added to the solution. In a 20 mL scintillation vial, the solution was heated to 120 °C for 24 h. The yellow-pink rectangular crystals were cooled to room temperature and kept in the mother solution.

The **Ho-BPDC-2** crystals were then washed with EtOH over a period of 6 days. New EtOH was added to replace the old EtOH once every 24 h.

 $C_{16}H_{22}FGdN_2O_8$  (Gd-BPDC-2). Gadolinium(III) nitrate pentahydrate (91.3 mg, 0207 mmol), BPDC (23.3 mg, 0.0876 mmol), and 2,6-difluorobenzoic acid (119.4 mg, 0.7552 mmols). Concentrated nitric acid (0.2 mL) was added to the solution. In a 20 mL scintillation vial, the solution was heated to 120 °C in an oven for 24 h. The white rectangular crystals were cooled to room temperature, centrifuged with DMF twice, and air-dried in an 80 °C oven. This resulted in a yield of 75.4%.

 $C_{16}H_{22}FTbN_2O_8$  (*Tb-BPDC-2*). Terbium(III) nitrate hexahydrate (185.2 mg, 0207 mmol), BPDC (54.4 mg, 0.0876 mmol), and 2-fluorobenzoic acid (486.7 mg, 0.7552 mmols). Concentrated nitric acid (0.4 mL) was added to the solution. In a 20 mL scintillation vial, the solution was heated to 120 °C in an oven for 24 h. The white rectangular crystals were cooled to room temperature, centrifuged with DMF twice, and air-dried in an 80 °C oven. This resulted in a yield of 72.5%.

#### ASSOCIATED CONTENT

# Supporting Information

The Supporting Information is available free of charge at https://pubs.acs.org/doi/10.1021/acs.inorgchem.3c03064.

PXRD patterns, EDS, XPS, gas adsorption, and magnetic data (PDF)

#### **Accession Codes**

CCDC 2090144–2090145 contain the supplementary crystallographic data for this paper. These data can be obtained free of charge via <a href="www.ccdc.cam.ac.uk/data\_request/cif">www.ccdc.cam.ac.uk/data\_request/cif</a>, or by emailing <a href="data\_request@ccdc.cam.ac.uk">data\_request/cif</a>, or by contacting The Cambridge Crystallographic Data Centre, 12 Union Road, Cambridge CB2 1EZ, UK; fax: +44 1223 336033.

# AUTHOR INFORMATION

# **Corresponding Author**

Kenneth J. Balkus, Jr — Department of Chemistry and Biochemistry, The University of Texas at Dallas, Richardson, Texas 75080, United States; ⊚ orcid.org/0000-0003-1142-3837; Email: Balkus@utdallas.edu

#### **Authors**

Marie L. Mortensen – Department of Chemistry and Biochemistry, The University of Texas at Dallas, Richardson, Texas 75080, United States

Shubham Bisht – Department of Chemistry and Biochemistry, Florida State University, Tallahassee, Florida 32306, United States

Muhammad Abbas — Department of Chemistry and Biochemistry, The University of Texas at Dallas, Richardson, Texas 75080, United States; orcid.org/0000-0001-6950-8986

Hamid Firouzi – Department of Chemistry and Biochemistry, The University of Texas at Dallas, Richardson, Texas 75080, United States

Gregory T. McCandless – Department of Chemistry and Biochemistry, The University of Texas at Dallas, Richardson, Texas 75080, United States

Michael Shatruk – Department of Chemistry and Biochemistry, Florida State University, Tallahassee, Florida 32306, United States

Complete contact information is available at: https://pubs.acs.org/10.1021/acs.inorgchem.3c03064

# **Author Contributions**

The manuscript was written through contributions of all authors. All authors have given approval to the final version of the manuscript.

#### **Funding**

Robert A. Welch Foundation (AT-1153) The University of Texas at Dallas Office of Research Core Facility Voucher Program (10319) National Science Foundation, Division of Chemistry (2300779).

#### Notes

The authors declare no competing financial interest.

#### ACKNOWLEDGMENTS

The authors would like to thank Simin Sheybani for helping with the <sup>1</sup>H NMR. The authors acknowledge support from the Robert A. Welch Foundation (Grant No. AT-1153). This project was also partially funded by The University of Texas at

Dallas Office of Research through the Core Facility Voucher Program (10319). Studies of magnetic properties were performed with support from the National Science Foundation (Grant CHE-2300779) and the Materials Characterization Laboratory (FSU075000MAC) at the Department of Chemistry and Biochemistry, Florida State University.

#### REFERENCES

- (1) Yaghi, O. M.; Li, H. Hydrothermal Synthesis of a Metal-Organic Framework Containing Large Rectangular Channels. *J. Am. Chem. Soc.* **1995**, *117*, 10401–10402.
- (2) Hoskins, B. F.; Robson, R. Design and Construction of a New Class of Scaffolding-like Materials Comprising Infinite Polymeric Frameworks of 3D-Linked Molecular Rods. A Reappraisal of the Zn(CN)<sub>2</sub> and Cd(CN)<sub>2</sub> Structures and the Synthesis and Structure of the Diamond-Related Frameworks [N(CH<sub>3</sub>)<sub>4</sub>] [Cu<sup>I</sup>Zn<sup>II</sup>(CN)<sub>4</sub>] and Cu<sup>I</sup>[4,4',4",4"'-Tetracyanotetraphenylmethane] BF<sub>4</sub>\*xC<sub>6</sub>H<sub>5</sub>NO<sub>2</sub>. *J. Am. Chem. Soc.* **1990**, *112* (4), 1546–1554.
- (3) Bhatt, P. M.; Belmabkhout, Y.; Assen, A. H.; Weseliński, ŁJ.; Jiang, H.; Cadiau, A.; Xue, D. X.; Eddaoudi, M. Isoreticular Rare Earth Fcu-MOFs for the Selective Removal of H<sub>2</sub>S from CO<sub>2</sub> Containing Gases. *Chem. Eng. J.* **2017**, 324, 392–396.
- (4) Angeli, G. K.; Loukopoulos, E.; Kouvidis, K.; Bosveli, A.; Tsangarakis, C.; Tylianakis, E.; Froudakis, G.; Trikalitis, P. N. Continuous Breathing Rare-Earth MOFs Based on Hexanuclear Clusters with Gas Trapping Properties. J. Am. Chem. Soc. 2021, 143 (27), 10250–10260.
- (5) Wei, N.; Zuo, R. X.; Zhang, Y. Y.; Han, Z. B.; Gu, X. J. Robust High-Connected Rare-Earth MOFs as Efficient Heterogeneous Catalysts for CO<sub>2</sub> Conversion. *Chem. Commun.* **2017**, *53*, 3224–3227.
- (6) Akbar, M. U.; Badar, M.; Zaheer, M. Programmable Drug Release from a Dual-Stimuli Responsive Magnetic Metal-Organic Framework. ACS Omega 2022, 7 (36), 32588–32598.
- (7) Marti, A. M.; Perera, S. D.; McBeath, L. D.; Balkus, K. J. Fabrication of Oriented Silver-Functionalized RPM3 Films for the Selective Detection of Olefins. *Langmuir* **2013**, *29* (19), 5927–5936.
- (8) Almáši, M.; Zeleňák, V.; Kuchár, J.; Bourrelly, S.; Llewellyn, P. L. New Members of MOF-76 Family Containing Ho(III) and Tm(III) Ions: Characterization, Stability and Gas Adsorption Properties. *Colloids Surf.* **2016**, 496, 114–124.
- (9) Santos, J. C. C.; Pramudya, Y.; Krstić, M.; Chen, D.-H.; Lilli Neumeier, B.; Feldmann, C.; Wenzel, W.; Redel, E. Halogenated Terephthalic Acid "Antenna Effects" in Lanthanide-SURMOF Thin Films. ACS Appl. Mater. Interfaces 2020, 12, 52166–52174.
- (10) N'Dala-Louika, I.; Ananias, D.; Latouche, C.; Dessapt, R.; Carlos, L. D.; Serier-Brault, H. Ratiometric Mixed Eu-Tb Metal-Organic Framework as a New Cryogenic Luminescent Thermometer. *J. Mater. Chem. C* **2017**, *5*, 10933–10937.
- (11) Thorarinsdottir, A. E.; Harris, T. D. Metal-Organic Framework Magnets. *Chem. Rev.* **2020**, *120*, 8716–8789.
- (12) Li, Y. J.; Wang, Y. L.; Liu, Q. Y. The Highly Connected MOFs Constructed from Nonanuclear and Trinuclear Lanthanide-Carboxylate Clusters: Selective Gas Adsorption and Luminescent PH Sensing. *Inorg. Chem.* **2017**, *56* (4), 2159–2164.
- (13) Deneff, J. I.; Rohwer, L. E. S.; Butler, K. S.; Valdez, N. R.; Rodriguez, M. A.; Luk, T. S.; Sava Gallis, D. F. Covert MOF-Based Photoluminescent Tags via Tunable Linker Energetics. *ACS Appl. Mater. Interfaces* **2022**, *14* (2), 3038–3047.
- (14) Chen, Z.; Weseliński, ŁJ.; Adil, K.; Belmabkhout, Y.; Shkurenko, A.; Jiang, H.; Bhatt, P. M.; Guillerm, V.; Dauzon, E.; Xue, D. X.; O'Keeffe, M.; Eddaoudi, M. Applying the Power of Reticular Chemistry to Finding the Missing Alb-MOF Platform Based on the (6,12)-Coordinated Edge-Transitive Net. *J. Am. Chem. Soc.* 2017, 139, 3265–3274.
- (15) Han, X.; Liu, J.; Yu, K.; Lu, Y.; Xiang, W.; Zhao, D.; He, Y. Water-Stable Eu<sub>6</sub> -Cluster-Based Fcu-MOF with Exposed Vinyl Groups for Ratiometric and Fluorescent Visual Sensing of Hydrogen Sulfide. *Inorg. Chem.* **2022**, *61*, 5067–5075.

- (16) Wei, W.; Wang, X.; Zhang, K.; Tian, C. B.; Du, S. W. Tuning the Topology from Fcu to Pcu: Synthesis and Magnetocaloric Effect of Metal-Organic Frameworks Based on a Hexanuclear Gd(III)-Hydroxy Cluster. *Cryst. Growth Des.* **2019**, *19*, 55–59.
- (17) Deacon, G. B.; Junk, P. C.; Kelly, R. P.; Wang, J. Exploring the Effect of the LnIII/LnII Redox Potential on C-F Activation and on Oxidation of Some Lanthanoid Organoamides. *Dalton Trans.* **2016**, 45 (4), 1422–1435.
- (18) Vizuet, J. P.; Mortensen, M. L.; Lewis, A. L.; Wunch, M. A.; Firouzi, H. R.; McCandless, G. T.; Balkus, K. J. Fluoro-Bridged Clusters in Rare-Earth Metal-Organic Frameworks. *J. Am. Chem. Soc.* **2021**, *143*, 17995–18000.
- (19) Li, H.-X.; Zhang, Z.-H.; Fang, H.; Xue, D.-X.; Bai, J. Synthesis, Structure and High Methane Storage of Pure D<sub>6</sub>R Yb(Y) Non-anuclear Cluster-Based Zeolite-like Metal—Organic Frameworks. *J. Mater. Chem. A* **2022**, *10*, 14795—14798.
- (20) Bicalho, H. A.; Saraci, F.; de Velazquez-Garcia, J. J.; Titi, H. M.; Howarth, A. J. Unravelling the Synthesis of a Rare-Earth Cluster-Based Metal-Organic Framework with Spn Topology. *Chem. Commun.* **2022**, 58, 10925–10928.
- (21) Ajoyan, Z.; Mandl, G. A.; Donnarumma, P. R.; Quezada-Novoa, V.; Bicalho, H. A.; Titi, H. M.; Capobianco, J. A.; Howarth, A. J. Modulating Photo- and Radioluminescence in Tb(III) Cluster-Based Metal-Organic Frameworks. *ACS Mater. Lett.* **2022**, *4*, 1025–1031.
- (22) Xia, H. L.; Zhou, K.; Guo, J.; Zhang, J.; Huang, X.; Luo, D.; Liu, X. Y.; Li, J. Amino Group Induced Structural Diversity and Near-Infrared Emission of Yttrium-Tetracarboxylate Frameworks. *Chem. Sci.* 2022, *13*, 9321–9328.
- (23) Abbas, M.; Maceda, A. M.; Firouzi, H. R.; Xiao, Z.; Arman, H. D.; Shi, Y.; Zhou, H. C.; Balkus, K. J. Fluorine Extraction from Organofluorine Molecules to Make Fluorinated Clusters in Yttrium MOFs. *Chem. Sci.* **2022**, *13*, 14285–14291.
- (24) Sheybani, S.; Abbas, M.; Firouzi, H. R.; Xiao, Z.; Zhou, H. C.; Balkus, K. J. Synthesis of Fluoro-Bridged Ho<sup>3+</sup> and Gd<sup>3+</sup> 1,3,5-Tris(4-Carboxyphenyl)Benzene Metal-Organic Frameworks from Perfluoroalkyl Substances. *Inorg. Chem.* **2023**, *62*, 4314–4321.
- (25) Liu, J.; Zhou, K.; Ullah, S.; Miao, J.; Wang, H.; Thonhauser, T.; Li, J. Precise Pore Engineering of Fcu-Type Y-MOFs for One-Step  $C_2H_4$  Purification from Ternary  $C_2H_6/C_2H_4/C_2H_2$  Mixtures. *Small* **2023**, *19*, No. 2304460.
- (26) Le, D. H.; Loughan, R. P.; Gładysiak, A.; Rampal, N.; Brooks, I. A.; Park, A. H. A.; Fairen-Jimenez, D.; Stylianou, K. C. Lanthanide Metal—Organic Frameworks for the Fixation of CO<sub>2</sub> under Aqueous-Rich and Mixed-Gas Conditions. *J. Mater. Chem. A* **2022**, *10*, 1442—1450.
- (27) Cheng, P. Lanthanide Metal-Organic Frameworks; Springer: Berlin, 2015; Vol. 163.
- (28) Abdulhalim, R. G.; Bhatt, P. M.; Belmabkhout, Y.; Shkurenko, A.; Adil, K.; Barbour, L. J.; Eddaoudi, M. A Fine-Tuned Metal-Organic Framework for Autonomous Indoor Moisture Control. *J. Am. Chem. Soc.* **2017**, *139* (31), 10715–10722.
- (29) Chen, H.; Yang, Z.; Do-Thanh, C. L.; Dai, S. What Fluorine Can Do in CO<sub>2</sub> Chemistry: Applications from Homogeneous to Heterogeneous Systems. *ChemSusChem* **2020**, *13*, 6182–6200.
- (30) Cadiau, A.; Belmabkhout, Y.; Adil, K.; Bhatt, P. M.; Pillai, R. S.; Shkurenko, A.; Martineau-Corcos, C.; Maurin, G.; Eddaoudi, M. Hydrolytically Stable Fluorinated Metal-Organic Frameworks for Energy-Efficient Dehydration. *Science* **2017**, *356*, 2023.
- (31) Christian, M. S.; Fritzsching, K. J.; Harvey, J. A.; Gallis, D. F. S.; Nenoff, T. M.; Rimsza, J. M. Dramatic Enhancement of Rare-Earth Metal—Organic Framework Stability Via Metal Cluster Fluorination. *JACS Au* **2022**, *2*, 1889—1898.
- (32) Vizuet, J. P.; Lewis, A. L.; McCandless, G. T.; Balkus, K. J. Holmium-Based Metal-Organic Frameworks Using the BDC Linker. *Polyhedron* **2021**, 205, No. 115283, DOI: 10.1016/j.poly.2021.115283.
- (33) Mortensen, M. L.; Lewis, A. L.; McCandless, G.; Balkus, K. J. Four Isostructural 3d-4f Mixed Metal Organic Frameworks and Their

Magnetic Properties. Crystals 2021, 11 (12), No. 1547, DOI: 10.3390/cryst11121547.

- (34) Kahn, O. Molecular Magnetism; VCH, 1993.
- (35) Regincós Martí, E.; Canaj, A. B.; Sharma, T.; Celmina, A.; Wilson, C.; Rajaraman, G.; Murrie, M. Importance of an Axial LnIII-F Bond across the Lanthanide Series and Single-Molecule Magnet Behavior in the Ce and Nd Analogues. *Inorg. Chem.* **2022**, *61*, 9906–9917.
- (36) Gagné, O. C. Bond-Length Distributions for Ions Bonded to Oxygen: Results for the Lanthanides and Actinides and Discussion of the f-Block Contraction: Results. *Acta Crystallogr., Sect. B: Struct. Sci., Cryst. Eng. Mater.* **2018**, 74, 49–62.
- (37) Brunet, G.; Habib, F.; Korobkov, I.; Murugesu, M. Slow Magnetic Relaxation Observed in Dysprosium Compounds Containing Unsupported Near-Linear Hydroxo- and Fluoro-Bridges. *Inorg. Chem.* **2015**, *54* (13), *6195*–*6202*.
- (38) Zhou, Q.; Yang, F.; Liu, D.; Peng, Y.; Li, G.; Shi, Z.; Feng, S. Synthesis, Structures, and Magnetic Properties of Three Fluoride-Bridged Lanthanide Compounds: Effect of Bridging Fluoride Ions on Magnetic Behaviors. *Inorg. Chem.* **2012**, *51* (14), 7529–7536.
- (39) Mínguez Espallargas, G.; Coronado, E. Magnetic Functionalities in MOFs: From the Framework to the Pore. *Chem. Soc. Rev.* **2018**, 47 (2), 533–557.
- (40) Zhang, X. J.; Su, F. Z.; Peng, Y.; Liu, C. S.; Sañudo, E. C. Lanthanide Chain Assembled in Metal—Organic Frameworks: Slow Relaxation of the Magnetization in Dy(III) and Er(III) Complexes. *Inorg. Chem. Commun.* **2019**, *102*, 30—34.
- (41) Wang, W.; Yan, L.-Q.; Cong, J.-Z.; Zhao, Y.-L.; Wang, F.; Shen, S.-P.; Zou, T.; Zhang, D.; Wang, S.-G.; Han, X.-F.; Sun, Y. Magnetoelectric Coupling in the Paramagnetic State of a Metal-Organic Framework. *Sci. Rep.* **2013**, *3*, No. 2024.
- (42) Luo, L. L.; Qu, X. L.; Li, Z.; Li, X.; Sun, H. L. Isostructural Lanthanide-Based Metal-Organic Frameworks: Structure, Photoluminescence and Magnetic Properties. *Dalton Trans.* **2018**, 47 (3), 925–934.
- (43) Doheny, P. W.; Cassidy, S.; Saines, P. Investigations of the Magnetocaloric and Thermal Expansion Properties of the Ln<sub>3</sub>(Adipate)<sub>4.5</sub>(DMF)<sub>2</sub> (Ln = Gd–Er) Framework Series. *Inorg. Chem.* **2022**, *61*, 4957–4964.
- (44) Zwanziger, C.; do Pim, W. D.; Kitos, A. A.; Ovens, J. S.; Pallister, P. J.; Murugesu, M. A Cationic Fcu-Lanthanide MOF Enhances the Uptake of Iodine Vapour at Room Temperature. *Chem. Commun.* **2022**, 58, 12700–12703, DOI: 10.1039/D2CC03299F.
- (45) Panagiotou, N.; Moscoso, F. G.; Lopes-Costa, T.; Pedrosa, J. M.; Tasiopoulos, A. J. 2-Dimensional Rare Earth Metal—Organic Frameworks Based on a Hexanuclear Secondary Building Unit as Efficient Detectors for Vapours of Nitroaromatics and Volatile Organic Compounds. *Inorg. Chem. Front.* **2022**, *9*, 4850–4863.
- (46) Loukopoulos, E.; Angeli, G. K.; Kouvidis, K.; Tsangarakis, C.; Trikalitis, P. N. Accessing 14-Connected Nets: Continuous Breathing, Hydrophobic Rare-Earth Metal Organic Frameworks Based on 14-c Hexanuclear Clusters with High Affinity for Non-Polar Vapors. ACS Appl. Mater. Interfaces 2022, 14, 22242–22251.
- (47) Ajoyan, Z.; Bicalho, H. A.; Donnarumma, P. R.; Antanovich, A.; Howarth, A. J. Tuning the Rare-Earth UiO-66 Metal-Organic Framework Platform for White Light Emission. *J. Mater. Chem. C* **2023**, *11*, 8929–8934.
- (48) Chakarova, K.; Strauss, I.; Mihaylov, M.; Drenchev, N.; Hadjiivanov, K. Evolution of Acid and Basic Sites in UiO-66 and UiO-66-NH<sub>2</sub> Metal-Organic Frameworks: FTIR Study by Probe Molecules. *Microporous Mesoporous Mater.* **2019**, 281, 110–122.
- (49) Planas, N.; Mondloch, J. E.; Tussupbayev, S.; Borycz, J.; Gagliardi, L.; Hupp, J. T.; Farha, O. K.; Cramer, C. J. Defining the Proton Topology of the Zr<sub>6</sub>-Based Metal-Organic Framework NU-1000. *J. Phys. Chem. Lett.* **2014**, *5* (21), 3716–3723.
- (50) Raiser, D.; Deville, J. P. Study of XPS Photoemission of Some Gadolinium Compounds. *J. Electron Spectrosc. Relat. Phenom.* **1991**, 57, 91–97.

- (51) Liu, Y.; Wang, Z. U.; Zhou, H.-C. Recent Advances in Carbon Dioxide Capture with Metal-Organic Frameworks. *Greenhouse Gases: Sci. Technol.* **2012**, *2*, 352–368.
- (52) Zouzou, A.; Beghidja, A.; Beghidja, C.; Guari, Y.; Larionova, J.; Long, J.; Gándara, F. Structural Diversity of Lanthanide Chain Compounds Based on 3-Ethoxycinnamate: Influence on the Magnetic Properties. *Cryst. Growth Des.* **2021**, *21* (9), 5072–5085.
- (53) Han, Y. F.; Zhou, X. H.; Zheng, Y. X.; Shen, Z.; Song, Y.; You, X. Z. Syntheses, Structures, Photoluminescence, and Magnetic Properties of Nanoporous 3D Lanthanide Coordination Polymers with 4,4'- Biphenyldicarboxylate Ligand. *CrystEngComm* **2008**, *10* (9), 1237–1242.
- (54) Carlin, R. L. Magnetochemistry; Springer: Berlin, Heidelberg, 1986. DOI: 10.1007/978-3-642-70733-9.
- (55) Corredoira-Vázquez, J.; González-Barreira, C.; Fondo, M.; García-Deibe, A. M.; Sanmartín-Matalobos, J.; Gómez-Coca, S.; Ruiz, E.; Colacio, E. Dinuclear Fluoride Single-Bridged Lanthanoid Complexes as Molecule Magnets: Unprecedented Coupling Constant in a Fluoride-Bridged Gadolinium Compound. *Inorg. Chem.* **2022**, *61* (26), 9946–9959.
- (56) Pedersen, K. S.; Lorusso, G.; Morales, J. J.; Weyhermüller, T.; Piligkos, S.; Singh, S. K.; Larsen, D.; Schau-Magnussen, M.; Rajaraman, G.; Evangelisti, M.; Bendix, J. Fluoride-Bridged  $\{Gd_3^{II}M_2^{III}\}$  (M = Cr, Fe, Ga) Molecular Magnetic Refrigerants. Angew. Chem., Int. Ed. **2014**, 53 (9), 2394–2397.
- (57) Rinehart, J. D.; Long, J. R. Exploiting Single-Ion Anisotropy in the Design of f-Element Single-Molecule Magnets. *Chem. Sci.* **2011**, *2*, 2078–2085.
- (58) Sheldrick, G. M. SHELXT—Integrated Space-Group and Crystal-Structure Determination. *Acta Crystallogr., Sect. A: Found. Adv.* **2015**, *71*, 3–8.
- (59) Sheldrick, G. M. Crystal Structure Refinement with SHELXL. Acta Crystallogr., Sect. C: Struct. Chem. 2015, 71, 3–8.